Dalton Transactions

An international journal of inorganic chemistry

This article can be cited before page numbers have been issued, to do this please use: P. Vargas, M. F. Venâncio, W. R. Rocha, S. A. Suarez and F. Doctorovich, *Dalton Trans.*, 2026, DOI: 10.1039/D6DT00559D.

ROYAL SOCIETY OF CHEMISTRY

rsc.li/dalton

View Article Online
DOI: 10.1039/D6DT00559D

ARTICLE

Reduction of nitric oxide to HNO by sodium dithionite: kinetics and mechanism

Received 00th January 20xx,
Accepted 00th January 20xx

DOI: 10.1039/x0xx00000x

Paola Vargas,[a] Mateus F. Venâncio,[b] Willian R. Rocha,[c] Sebastián A. Suarez,[d,†] Fabio A. Doctorovich.[a,†]

16-digit ORCID of the author(s): 0000-0002-9832-6097, 0000-0002-8088-447X, 0000-0002-0025-2158, 0000-0003-0236-5743, 0000-0003-1088-2089

Sodium dithionite is a widely used reductant in biochemical and industrial applications, yet its intrinsic instability and complex redox chemistry continue to pose challenges for mechanistic interpretation. One relatively underexplored aspect is its reactivity with nitric oxide (NO•), a small redox-active signalling molecule. While dithionite is commonly employed to reduce metal centres in enzymes, its potential interaction with NO• may influence experimental outcomes in aqueous redox systems. Here, we show that under anaerobic, near-neutral aqueous conditions, dithionite reacts with NO• leading to the formation of azanone (HNO, nitroxyl), the one-electron-reduced and protonated congener of nitric oxide. Formation of HNO is supported by direct trapping experiments using Mn(III) porphyrins and by indirect detection of N_2O, a characteristic product of HNO dimerization. These findings reveal a previously overlooked route for HNO generation in dithionite-containing systems and highlight potential artefacts in biochemical experiments involving NO• and strong reductants, particularly in studies probing thiol reactivity or metalloprotein function.

Introduction

Sodium dithionite ($Na_2S_2O_4$) is widely used in industry and laboratory chemistry and remains a convenient reductant in biochemical research, particularly for accessing reduced states of metalloenzymes and enzyme complexes.[1,2] In aqueous solution, this reductant can act either as the dimer $S_2O_4^{2-}$ or through its radical dissociation product $SO_2^{\bullet-}$, which coexist in equilibrium (Eq. 1). The presence of the $SO_2^{\bullet-}$ radical in dithionite solutions was established by EPR spectroscopy,[3] and the homolysis is endothermic, with an equilibrium constant that increases with temperature ($K_H \approx 1.4 \times 10^{-9}$ at 298 K).[4]

$$S_2O_4{}^{2-} \underset{k_{-h}}{\overset{k_h}{\rightleftarrows}} 2SO_2{}^{\bullet-} \qquad \text{(Eq.1)}$$

The redox behaviour of dithionite solutions is therefore strongly dependent on concentration and speciation. Mayhew and co-workers rationalized the dithionite/(bi)sulfite redox chemistry by considering $SO_2^{\bullet-}$ as the effective reducing species and estimated a midpoint redox potential of E′ ≈ −0.66 V for the $SO_2^{\bullet-}/HSO_3^-$ couple at pH 7 and 25 °C, with less negative values at higher dithionite concentrations where the dimer predominates.[5] This chemistry is also closely linked to the intrinsic instability of dithionite. In the presence of oxygen, it is rapidly oxidized to (bi)sulfite and (bi)sulfate (Eq. 2),[6,7] while under anaerobic conditions it decomposes to (bi)sulfite and thiosulfate (Eq. 3).[8]

$$Na_2S_2O_4 + O_2 + H_2O \rightarrow NaHSO_4 + NaHSO_3 \qquad \text{(Eq.2)}$$

$$2Na_2S_2O_4 + H_2O \rightarrow 2NaHSO_3 + Na_2S_2O_3 \qquad \text{(Eq.3)}$$

The kinetics of these processes are highly sensitive to pH, temperature, and concentration, as documented in a wide range of experimental studies.[9–14] Consequently, the reactivity of dithionite must be evaluated under the specific conditions employed in a given experiment to ensure reliable mechanistic interpretation.

---

[a] Departamento de Química Inorgánica, Analítica, y Química Física, Facultad de Ciencias Exactas y Naturales, Universidad de Buenos Aires, INQUIMAE-CONICET. Ciudad Universitaria, Pab. 2, Piso 3, C1428EHA Buenos Aires, Argentina.
[b] Laboratório de Termodinâmica, Espectroscopia e Cinética, LaTEC, Universidade Federal da Bahia, Instituto de Química, Departamento de Físico-Química, Salvador, Bahia, 40170-110, Brazil.
[c] Laboratório de Estudos Computacionais em Sistemas Moleculares, eCsMo^{Lab}, Departamento de Química – ICEX, Universidade Federal de Minas Gerais, Belo Horizonte, Minas Gerais, 31270-901, Brazil.
[d] Departamento de Química Analítica y Análisis Instrumental. Facultad de Ciencias. c/Francisco Tomás y Valiente, No 7. Campus de Excelencia de la Universidad Autónoma de Madrid, Madrid 28049. Spain.
† *sebastian.suarez@uam.es , doctorovich@qi.fcen.uba.ar

Supplementary Information available: See DOI: 10.1039/x0xx00000x

View Article Online
DOI: 10.1039/D6DT00559D

In biochemical contexts, dithionite is routinely used at millimolar concentrations to generate reduced metalloprotein states,[1,15–17] including numerous nitrosylated heme proteins systems in which it is often assumed to be chemically non-innocent.[18–20] However, increasing evidence indicates that this reductant can participate directly in side reactions at higher concentrations.[21] Moreover, dithionite has been used explicitly as a scavenger of nitric oxide (NO•).[22] Early work by Moore and Gibson reported measurable reaction kinetics between dithionite and NO•,[23] and dithionite has subsequently been employed to remove NO• released from proteins such as neuroglobin in ligand-exchange and redox studies.[24,25] The possibility that dithionite directly consumes NO• is also relevant in enzymatic systems where NO• is generated *in situ*. For example, in the reduction of nitrite by cystathionine β-synthase (CBS), variations in dithionite concentration were shown to modify the observed kinetics, consistent with competition between CBS-Fe(II) and dithionite for NO• (Eqs. 4-6).[26] Importantly, nitrite itself is not reduced by dithionite,[27] supporting the idea that such effects arise from reactions involving NO• rather than upstream nitrite chemistry.

$$\mathrm{CBS-Fe(II)+NO_2^-+H^+\rightarrow CBS-Fe(III)+\bullet CBS+OH^-}\qquad \text{(Eq.4)}$$

$$\mathrm{CBS-Fe(III)+e^-\rightarrow CBS-Fe(II)}\qquad \text{(Eq.5)}$$

$$\mathrm{CBS-Fe(II)+NO\bullet\ \leftrightarrow CBS-Fe(II)NO^{\bullet}}\qquad \text{(Eq.6)}$$

From a redox perspective, reducing or hypoxic environments are expected to favour the conversion of NO• into more reduced nitrogen species. In this context, the one-electron reduction and protonation of NO• yields azanone (HNO, nitroxyl).[28–31] HNO exhibits chemical reactivity that is distinct from that of its redox congener NO• and has attracted considerable interest.[32–41] This molecule is highly unstable, precluding storage and necessitating the use of donor compounds such as Angeli's salt.[42–44] Recent studies have demonstrated that NO• can be converted to HNO by relatively mild reductants such as hydrogen sulfide, aromatic alcohols, and thiols, including cysteine.[45,46] In addition, an innovative study demonstrated the endogenous generation of HNO in plants, which is achieved through the reduction of NO•.[46] Given the high reactivity of HNO towards thiols and its potential to alter enzymatic function,[47–49] the possibility that sodium dithionite may directly reduce NO• becomes particularly relevant. In this work, we investigate the anaerobic reaction between sodium dithionite and NO•, combining kinetic measurements, spectroscopic detection, and DFT calculations to demonstrate that dithionite converts NO• to HNO under aqueous, near-neutral conditions.

Experimental section

Reagents. Sodium hydrosulfite (dithionite) was purchased from Sigma-Aldrich. Water-soluble manganese(III) meso-tetrakis(N-ethylpyridinium-2-yl) porphyrin (Mn(III)TEPyP) was purchased from Frontier Scientific (Scheme S1). Trioxodinitrate (Angeli's salt, $N_2O_3^{2-}$) was synthesized according to published procedures.[42,43] NO• was generated anaerobically according to published procedures from $NaNO_2$, $FeSO_4$, and NaBr and purified by passage through 0.25 M NaOH to remove higher nitrogen oxides.[50] Milli-Q grade water and high-purity argon were used in all experiments. Unless otherwise stated, all experiments were performed at 25 °C in 0.1 M phosphate buffer, pH = 7.25, containing 10^{-4} M EDTA to avoid interferences or unwanted reactions by Cu(II) or other divalent cations.

Preparation of anaerobic solutions. At 25 °C, the solubility of molecular oxygen (O_2) in water is 1.27 mM·atm^{-1}; under ambient air ($pO_2 \approx 0.21$ atm), this corresponds to an equilibrium concentration of approximately 0.26 mM.[51]

All aqueous solutions were rendered anaerobic by purging with high-purity argon for at least 30 min prior to use and were handled using gastight syringes and septum-sealed vessels. Sodium dithionite solutions were freshly prepared immediately before each experiment to minimise decomposition. The solid dithionite was degassed by repeated vacuum–argon cycles, then dissolved in a previously degassed buffer, and the resulting solutions were stored under an inert atmosphere in a Schlenk tube. Nitric oxide solutions were prepared by bubbling purified NO• gas into degassed water under anaerobic conditions to obtain a saturated aqueous solution. The concentration of the saturated NO• solution was taken as 1.94 mM at 25 °C, in accordance with reported solubility data.[52] All kinetic measurements were performed under continuous stirring to ensure rapid homogenisation after the addition of NO•. Control experiments and product analysis did not indicate the formation of nitrite or nitrate under the anaerobic conditions employed.

Fourier Transform Infrared (FTIR) Spectroscopy (Transmission). Gas-phase infrared spectra were recorded in transmission using a fixed-volume sealed FTIR gas cell equipped with NaCl windows (Thermo Nicolet). The formation of nitrous oxide (N_2O) was monitored via its characteristic asymmetric stretching band at 2212 cm^{-1} and 2236 cm^{-1}.[53–56] In a typical experiment, the reaction between dithionite and NO• was carried out in a total volume of 10 ml of solution in 100 ml flasks. The dithionite solution was prepared directly in the flasks, for which the required amount of solid was weighed and purged by emptying/filling cycles with high-purity argon. The solid was dissolved with the required volume of the buffer, added with a glass syringe. The saturated solution of NO• in H_2O was then injected and allowed to react for a specified time.

Although N_2O exhibits significant solubility in water, the large headspace-to-solution volume ratio employed in the experimental setup (ca. 90 mL gas over 10 mL solution) promotes efficient partitioning of N_2O into the gas phase over the course of the reaction. As a result, substantial amounts of N_2O accumulate in the headspace and can be readily detected by infrared spectroscopy.

All spectra were acquired using identical total gas volumes, with argon employed as an inert balance when required, ensuring comparable pressure conditions and enabling quantitative

View Article Online
DOI: 10.1039/D6DT00665D

comparison between experiments. Under this setup, the nitrous oxide signals for each injection were compared with a calibration curve prepared by injecting samples of N_2O produced *in situ* by the decomposition of Angeli's salt.

Attenuated Total Reflectance Fourier Transform Infrared (ATR-FTIR) spectroscopy. The ATR-FTIR spectra for detecting the final sulfur product were recorded using a Thermo Nicolet 8700 FTIR spectrophotometer equipped with a Smart Orbit detector and a diamond crystal plate. For each sample, a background spectrum was recorded prior to sample deposition, after which 50 µL of the solution was applied to the crystal surface. All ATR-FTIR measurements were performed under aerobic conditions. To identify the final sulfur-containing products, the reaction between dithionite and NO• was carried out by bubbling NO• gas into an anaerobic 0.2 M dithionite solution for 15 min, after which the ATR-FTIR spectrum was recorded.

UV-visible spectroscopy. Measurements were recorded using an HP/Agilent 8453 spectrophotometer in a 1 cm path length quartz cuvette, with the respective buffer solutions used as blanks. The inert atmosphere was achieved by applying a flow of pure argon inside the cuvette, which was perfectly sealed with septa.

Anaerobic degradation of dithionite. The anaerobic degradation of 10 mM dithionite was measured following the absorption at 315 nm by UV-visible spectroscopy for 6 hours, with spectra taken every 15 seconds. These data were analysed to calculate the order of reaction and the value of the rate constant.

System for the direct detection of HNO by trapping with Mn(III)TEPyP porphyrin. HNO reacts readily with Mn(III) porphyrins, including Mn(III)TEPyP, to form the corresponding nitrosylated Mn-NO complex, which is characterized by a pronounced blue shift of the Soret band of approximately 30 nm.[57–59] In contrast, nitric oxide does not react directly with Mn(III) porphyrins under these conditions. This selectivity makes Mn(III)TEPyP a suitable trapping agent for HNO detection. Importantly, the formation of the Mn-NO complex is a cumulative process, enabling quantitative detection of HNO generated over time even when its instantaneous steady-state concentration is low.

However, Mn(III)TEPyP is readily reduced by strong chemical reductants to Mn(II), which reacts rapidly with NO• to form the same Mn–NO species.[59–61] Consequently, when dithionite, NO•, and the porphyrin are present in the same solution, direct discrimination between NO• and HNO-derived signals becomes impossible. To overcome this limitation, HNO generation and detection were spatially decoupled by performing the reaction between dithionite and NO• in a vessel physically separated from the Mn(III)TEPyP solution, followed by transfer of the gaseous reaction products to the porphyrin-containing solution for UV–visible detection. The experimental configuration used for this purpose is shown schematically in Figure 1.

In this setup, NO• was generated anaerobically in **part 1** by dropwise addition of degassed water to a mixture of $NaNO_2$, $FeSO_4$, and NaBr. The resulting gas stream was passed through an aqueous NaOH solution (**part 2**) to remove higher nitrogen oxides, such as NO_2. The purified gas was then introduced into the reaction vessel containing dithionite (**part 3**), where HNO was generated, and finally directed into the Mn(III)TEPyP solution (**part 4**). In this final compartment, HNO was trapped cumulatively as the Mn-NO complex and monitored by UV–visible spectroscopy.

This multicompartmental design decouples HNO generation from detection, preventing reductive interference by dithionite while enabling cumulative trapping of gaseous HNO prior to dimerization.

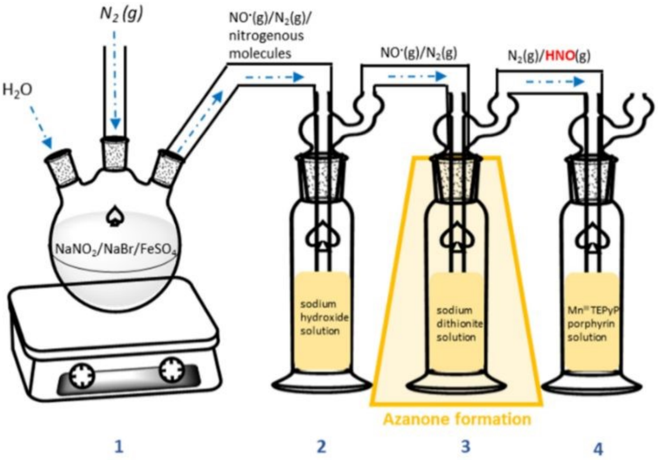

Fig.1 - Anaerobic multicompartmental system for the detection of HNO by trapping with Mn(III) porphyrins. The experimental setup consists of four physically separated compartments that decouple HNO generation from detection. (1) Nitric oxide (NO•) is generated anaerobically from $NaNO_2/FeSO_4/NaBr$. (2) The gas stream is passed through an aqueous NaOH solution (0.25 M) to remove higher nitrogen oxides. (3) Purified NO• reacts with sodium dithionite (3.3 mM), leading to the formation of reduced nitrogen species. (4) Gaseous products are transferred into a Mn(III)TEPyP solution (1 µM), where HNO is trapped cumulatively as the Mn–NO complex and detected by UV–visible spectroscopy.

Computational details. All the geometries presented in this work were optimized without any constraints under the Density Functional Theory (DFT) formalism using the meta-GGA r^2-SCAN exchange-correlation density functional with the Ahlrichs' def2-TZVPP basis set.[62] London dispersion interactions were also employed through Grimme's D4 correction.[63] Solvent effects were simulated using Truhlar's Universal Solvation Model (SMD).[64] This level of theory will be referred to as r^2-SCAN(D4)/Def2-TZVPP(SMD). Frequency calculations were also performed under the harmonic oscillator model to ensure that the optimized geometries are true minima or a transition state. A true minimum is characterized by the absence of imaginary frequencies, while one imaginary frequency indicates a transition state. All quantum chemical calculations were performed using the ORCA 5.0.3 version.[65]

View Article Online
DOI: 10.1039/D6DT00559D

Results and discussion

Direct HNO detection. As described in the Materials and Methods section, Mn(III) porphyrins such as Mn(III)TEPyP selectively react with HNO to form the corresponding Mn–NO complex, which accumulates over time and exhibits a characteristic blue shift of the Soret band of approximately 30 nm.[57–59] This cumulative trapping behaviour enables the detection of low steady-state fluxes of HNO generated in the gas phase.

When the gas mixture produced in the multicompartmental system shown in **Fig. 1** was bubbled into the Mn(III)TEPyP solution, a progressive spectral transformation was observed. After 40 min of contact with the NO•/N_2 gas stream, an isosbestic point was clearly evidenced together with the growth of a new Soret band at 434 nm, characteristic of the Mn–NO complex (**Fig. 2A**). The continuous increase of this band over time reflects the cumulative formation of the Mn–NO• species and confirms the generation of HNO from the reaction between dithionite and NO•.

Control experiments were performed to validate the specificity of the detection system. In the absence of NO•, achieved by bubbling N_2 through the system while omitting the NO• generation vessel (**Fig. 2B**), no formation of the Mn–NO complex was observed, even after 120 min of continuous gas flow. Similarly, when the dithionite-containing vessel was removed and a NO•/N_2 mixture was passed directly through the system (**Fig. 2C**), no spectral changes associated with Mn–NO formation were detected. These controls demonstrate that both NO• and dithionite are required to generate HNO under the experimental conditions employed.

End nitrogen product detection. HNO undergoes dimerization to form hyponitrous acid ($H_2N_2O_2$), which subsequently decomposes to nitrous oxide (N_2O) and water. This process follows second-order kinetics (k = 8 x 10^6 $M^{-1}s^{-1}$),[30] such that the rate of N_2O formation depends strongly on the instantaneous local concentration of HNO. Consequently, even when the rate constant for dimerization is relatively large, the effective rate of N_2O formation can be low under conditions where HNO is generated slowly, and its steady-state concentration remains small. While HNO has signals in the IR range,[66,67] it is challenging to detect using this technique due to its short lifetime. Because N_2O is a gaseous species readily detected by infrared spectroscopy, exhibiting a characteristic asymmetric stretching band in the 2212–2236 cm^{-1} region,[53–56] it is commonly employed as an indirect marker for HNO formation.[53–55] To monitor N_2O formation during the reaction between sodium dithionite and NO•, the anaerobic reaction was carried out, and the amount of N_2O released to the gas phase was quantified using an Angeli's salt calibration. During the reaction between 6 mM dithionite and 400 µM NO• (4 µmol), the amount of N_2O detected in the headspace increases with time following an initial induction period (**Fig. 2D**).

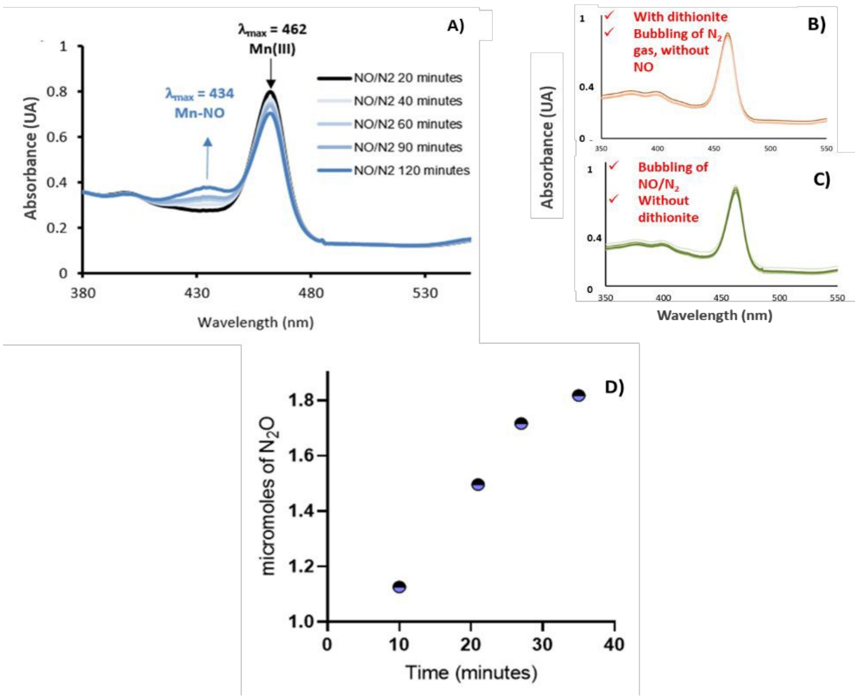

Fig.2 – Direct detection of HNO by cumulative trapping with Mn(III)TEPyP. A) UV–visible spectra of Mn(III)TEPyP recorded at different times during bubbling of the NO•/N_2 gas mixture generated in the system shown in Fig. 1, showing the progressive formation of the Mn–NO complex with a characteristic Soret band at 434 nm. B) Control experiment in which N_2 was bubbled through the system of Fig. 1 with the NO• generation vessel (part 1) omitted. C) Control experiment in which a NO•/N_2 gas mixture was bubbled through the system of Fig. 1 with the dithionite-containing vessel (part 3) omitted. D) Formation of N_2O (µmol) as a function of reaction time during the reaction between dithionite (6 mM) and NO• (400 µM).

View Article Online
DOI: 10.1039/D6DT00559D

During the initial ca. 10 min of the experiment, the detected N_2O signal remains approximately constant. This induction period is attributed to a combination of factors, including the second-order dependence of HNO dimerization on its local concentration, the partitioning of N_2O between the aqueous phase and the gas phase, and the time required for N_2O generated in solution to transfer into the headspace. Moreover, the delayed formation of N_2O is discussed below in terms of intermediate species and competing pathways that are consistent with both the experimental kinetic data and the computational results.

After this initial period, a steady increase in the amount of N_2O detected is observed. Under these conditions, the minimum amount of N_2O detected was 1.1 µmol, corresponding to a detection limit of 1.6 ppm, while 1.8 µmol of N_2O was detected in the headspace after 35 min of reaction. Considering the reaction stoichiometry, this observation indicates that 90% of the nitrogen initially introduced as NO• is recovered as N_2O, identifying N_2O as the dominant nitrogen-containing end product detected under these conditions.

While alternative pathways cannot be excluded, the combined detection of N_2O as the predominant nitrogen product and the kinetic behaviour observed provide independent support for the involvement of HNO as a key intermediate in the reaction between dithionite and NO•.

End sulfur products detection. The identity of the final sulfur-containing products formed during the reaction between sodium dithionite and NO• was investigated by ATR-FTIR spectroscopy. In a first step, reference ATR-FTIR spectra of several sulfur species that could plausibly arise from dithionite transformation under the experimental conditions were recorded (**Fig. S1**). These reference spectra were subsequently compared with that obtained after reaction of dithionite with NO•.

The reaction was carried out by passing a flow of freshly generated NO• through a 0.2 M aqueous sodium dithionite solution for 15 min. The resulting reaction mixture was then analysed by ATR-FTIR spectroscopy. Among all sulfur-containing species examined, sodium metabisulfite ($Na_2S_2O_5$) was the only compound whose ATR-FTIR spectrum matched that of the reaction mixture, with coincident band positions and relative intensities (**Fig. 3**). This spectral agreement identifies sodium metabisulfite as a major end sulfur product of the reaction between sodium dithionite and NO• under the conditions employed.

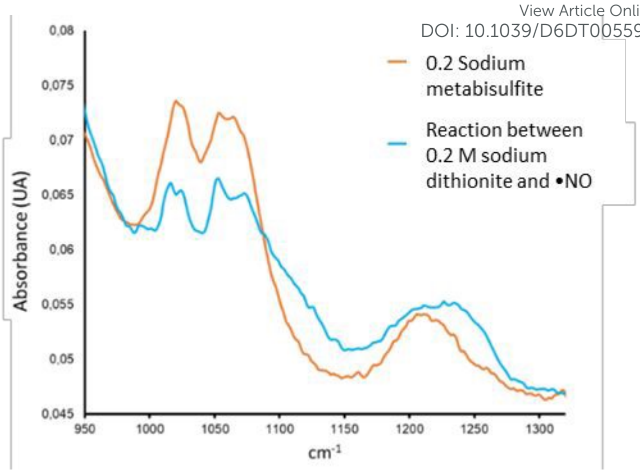

Fig.3 - Comparison between the ATR-FTIR spectrum of sodium metabisulfite (orange, 0.2 M) and that obtained after reaction of sodium dithionite (light blue, 0.2 M) with NO•, showing coincident band positions in the characteristic S–O stretching region.

Based on the combined nitrogen and sulfur product analyses, a global reaction consistent with the experimental observations can be proposed, in which dithionite is converted into metabisulfite with concomitant formation of N_2O as the nitrogen-containing end product (Eq. 7). The mechanistic implications of this transformation are discussed in detail below.

$$Na_2S_2O_4 + 2(NO\bullet) \rightarrow Na_2S_2O_5 + N_2O \qquad \text{(Eq.7)}$$

Kinetics of the reaction by UV-visible spectroscopy

As discussed above, dithionite concentration can be determined from the UV-visible spectrum (**Fig. 4**). Taking these data into account, the absorbance at 315 nm of a dithionite solution was measured every 180 s, from the addition of a specific volume of an aqueous solution of NO•. From these measurements, kinetic traces describing the decay of dithionite concentration upon reaction with NO• were obtained.

Under conditions where NO• was not present in large excess relative to dithionite, the decay of the dithionite concentration could be reasonably described by a pseudo-first-order behaviour (**Fig. 4B,C**), with an apparent rate constant of 1.7 × 10^{-3} s^{-1} (k′⍰, Eq. 8). A mechanistic scenario compatible with this behaviour involves the slow generation of sulfur-centered radical species, such as $SO_2\bullet^-$, followed by rapid reaction with NO• (Eq. 9, **Fig. 5**). Since reactions between radical species are typically fast and may approach diffusion-controlled limits,[68–71] this behaviour is consistent with pseudo-first-order kinetics when NO• is not present in excess. This description, however, does not imply that this pathway is exclusive under all experimental conditions. For example, under these conditions, we disregard the dimerization reaction between the $SO_2^{\bullet-}$ radical monomers because the $SO_2^{\bullet-}$ radicals themselves are present at such a low concentration that they would most likely react with excess NO•. The rate equations for these reactions are:

View Article Online
DOI: 10.1039/D6DT00659D

$$S_2O_4{}^{2-}\xrightarrow{k_{h'}}2SO_2{}^{\bullet-} \qquad \text{(Eq. 8)}$$

$$SO_2{}^{\bullet-} + NO\bullet + H_3O^+\xrightarrow{k_2}SO_2 + HNO + H_2O \qquad \text{(Eq.9)}$$

$$-\frac{d\,[S_2O_4{}^{2-}]}{dt} = k_{h'}[S_2O_4{}^{2-}] \qquad \text{(Eq.10)}$$

$$\frac{d\,[SO_2{}^{\bullet-}]}{dt} = \frac{1}{2}k_{h'}[S_2O_4{}^{2-}] - k_2[SO_2{}^{\bullet-}][NO\bullet] \qquad \text{(Eq.11)}$$

So, if we apply steady state to Eq.11, since the monomer is formed by homolysis and is consumed by reaction with NO•, and we rearrange,

$$0 = \frac{1}{2}k_{h'}[S_2O_4{}^{2-}] - k_2[SO_2{}^{\bullet-}][NO\bullet] \qquad \text{(Eq. 12)}$$

$$k_{h'}[S_2O_4{}^{2-}] = 2k_2[SO_2{}^{\bullet-}][NO\bullet] = v \qquad \text{(Eq. 12´)}$$

As derived from the mechanism, the rate equation is compatible with an order 1 in dithionite (**Fig. 5**). As noted above, HNO undergoes dimerization forming $H_2N_2O_2$ (equation 13), which typically decomposes to yield N_2O and H_2O.[54]

$$2HNO \rightarrow cis-H_2N_2O_2 \rightarrow cis-HN_2O_2{}^- + H^+ \qquad \text{(Eq.13)}$$

In this context, the kinetics results of **Fig. 4** are consistent with what is observed in **Fig. 2D** for N_2O production. Another reaction that could be present in the medium is the reaction between HNO and NO• to form the radical $HN_2O_2\bullet$, with N_2O and $NO_2{}^-$ as the initial products, ultimately leading to the final products. However, no formation of $NO_2{}^-$ was detected by ion exchange chromatography under the experimental conditions employed, indicating that this pathway is unlikely to contribute significantly under these conditions. It is important to remark that the planar intermediate $H_2N_2O_2$ exhibits two isomers, designated as *cis*-ON(H)N(H)O and *trans*-ON(H)N(H)O, due to a specific double bond character between the nitrogen atoms. Once the dimer is formed, *cis-trans* isomerization becomes kinetically prohibited. However, the formation of the N_2O product occurs via two primary pathways involving *cis*-hyponitrous acid and its conjugate base. Furthermore, under aqueous, near-neutral conditions, there is a clear preference for the anionic pathway.[72]

In contrast, when NO• was added in excess with respect to dithionite, the kinetic behaviour changed markedly. In this case, attempts to fit the initial portion of the kinetic traces using simple linear or exponential models were unsuccessful, even within the first seconds after the reaction started (**Fig. S2** and **Fig. S3**). This behaviour indicates that the reaction cannot be adequately described by a single elementary rate law (zero-, first-, or second-order) when the relative concentrations of the reactants change. These observations are consistent with the involvement of multiple, rapidly interconverting nitrogen- and sulfur-centered intermediates, whose relative contributions depend on the experimental conditions. Accordingly, a more detailed and phenomenological treatment of the kinetic data was required (see SI **Fig. S4–11**).

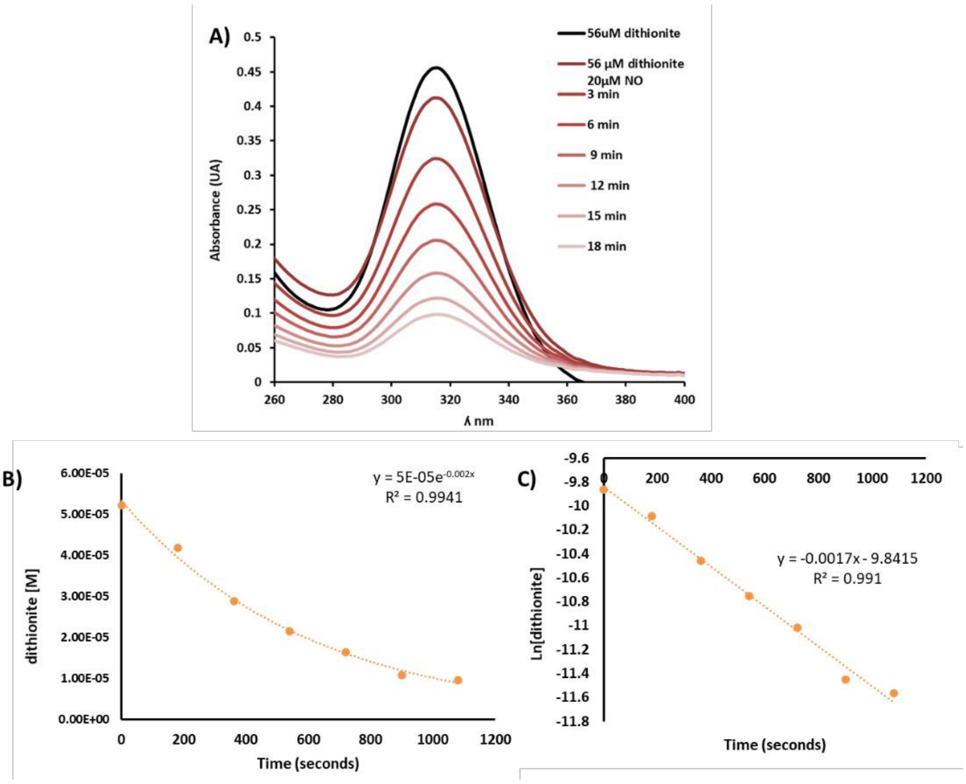

Fig.4 - A) UV-visible absorbance spectra of 56 µM dithionite at different times after addition of a 100 µM anaerobic NO• solution. **B)** The decay of the dithionite concentration due to its reaction with NO•. **C)** The natural logarithm of the dithionite concentration over time. UV–visible spectra were continuously acquired at 5 s intervals over the entire reaction time; for visual clarity, only representative points are displayed in the plots.

View Article Online
DOI: 10.1039/D6DT00559D

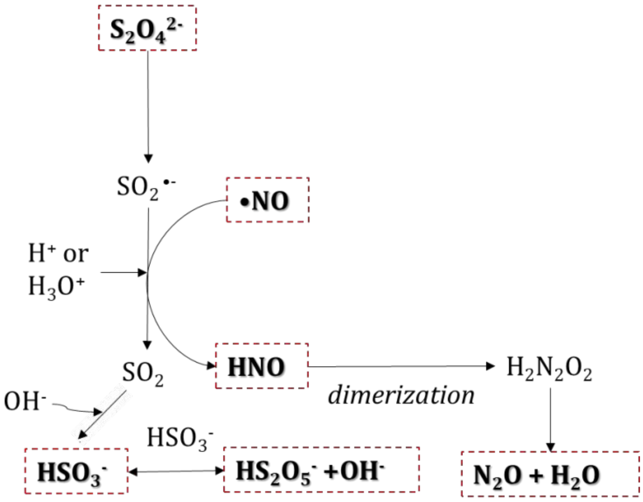

Fig. 5. Proposed mechanism. These results are interpreted in terms of a reaction network of chemically compatible pathways rather than a single, strictly sequential mechanism. See also **Fig. S6**

In addition, the equilibrium constant (K_H) was estimated by computational analysis with dimer and monomer alone or in the presence of Na^+, K^+, and Ca^{2+}. Although the equilibrium constant (K_H) was slightly lower in the presence of the cations, there were no significant differences between them, the error being within 1% for all.

Moreover, the Solvent Kinetic Isotope Effect (SKIEs) was analysed (see SI for a detailed discussion). Although the kinetics observed when D_2O was used instead of H_2O showed that the effective rate of dithionite consumption by NO• was accelerated due to the solvent change ($k_{H2O}/k_{D2O} \approx 0.60$, see **Fig. 6**), the concentrations of the protonated species present are very low at the pH of the experiments. However, the $SO_2^{\bullet-}$ radical could interact more strongly with D_2O since the *deuterium bridging* (with D_2O) is stronger than its H_2O counterpart. Consequently, the intermediate stabilizes, which results in an increase in the net reaction rate (k_1).

In addition, N_2O formation also showed an inverse isotope effect, with a similar ratio ($H_2O/D_2O \approx 0.62$ at 30 minutes, **Fig. S12A**). While isotopic substitution in HNO itself could, in principle, influence downstream chemistry, calculations comparing the dimerization of HNO vs DNO suggest only a minor energetic difference (**Fig. S12B**). Taken together, these observations suggest that the dominant origin of the inverse isotope effect lies in the initial stages of the mechanism and is then propagated to the final N_2O readout. This interpretation is consistent with the rate-controlling step identified by the kinetic analysis (Eq. 12/12′), while HNO dimerization is expected to be fast under the conditions employed.

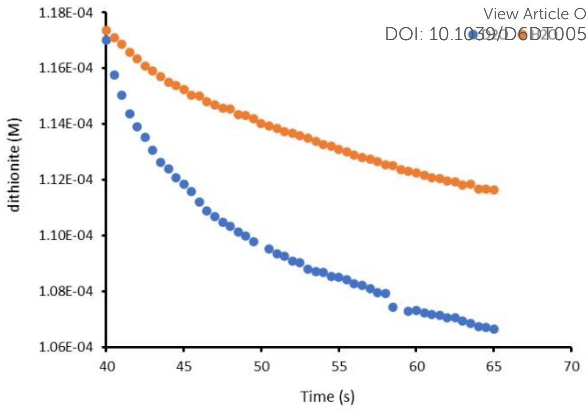

Fig.6 - D_2O vs H_2O experiments. A) [Dithionite] vs. time after mixing 100 µM of NO• with 118 µM of dithionite under anaerobic conditions using H_2O (orange) or D_2O (blue) as solvent.

One important aspect to consider is the reaction between dithionite and O_2.[71,73–75] Although all the experiments were carried out in a strictly anaerobic manner, traces of this gas may remain in the system, so the possibility that this reaction is present should be analysed. This is a very fast reaction, leading to the rate-limiting step being the dissociation of the dithionite (Eq.1).[6,7] If the UV-visible spectrum of an anaerobic solution of dithionite is analysed at the moment when oxygenated H_2O is added, an instantaneous disappearance of the band corresponding to the absorption maximum of dithionite at 315 nm is observed. The solubility of O_2 in water is 1.46 mM at 0 °C, 1.27 mM at 25 °C, and approximately 1.09 mM at 35 °C, corresponding to slightly more than 50 % of the solubility of NO• (1.94 mM).[51,76] However, O_2 solubility scales with its molar fraction in the gas phase. Under normal atmospheric conditions (pO_2 = 0.21 atm), the effective solubility is reduced to approximately 0.25 mM. Although NO• is diluted by adding it to the dithionite solution, O_2 is also diluted. For this reason and considering the strict anaerobic conditions used in the experiments, the reaction between dithionite and oxygen was not included in the kinetic analysis.

Finally, analysis does not include the decomposition of dithionite *per se*, since the rate at which it occurs is negligible compared to the rate at which it reacts with NO. The anaerobic decomposition kinetics of dithionite were measured at a pH of 7.25 and room temperature (**Fig. S13** and **Fig. S14**). The data are consistent with a second-order reaction, with a rate constant of 22.92 M^{-1} min^{-1}. Although it is not possible to directly compare this data with those reported in the bibliography, due to the variability of the experimental conditions (concentration, temperature, and pH), in general, there is an agreement that the reaction is slow at pH levels above 6 and at low dithionite concentrations.[13] Consistent with this behaviour, deviations from the general kinetic trends were observed under conditions of extreme pH values and low dithionite concentrations. However, as the reaction rate under these conditions is significantly reduced, these effects were considered negligible in the general analysis of the reaction between dithionite and NO•.

Computational Results

To evaluate the thermodynamic and kinetic feasibility of chemically compatible reaction pathways within the network shown in Fig. 5, a computational analysis was performed at the r²-SCAN(D4)/def2-TZVPP(SMD) level of theory.

As discussed above, dithionite in solution undergoes reversible homolysis, leading to the formation of sulfur-centered radical species such as $SO_2•^-$, with an equilibrium constant of 1.4×10^{-9}. Accordingly, HNO generation can be explored by considering reactions involving $SO_2•^-$ and NO•. Accordingly, we investigated a representative pathway for HNO formation in the presence of a Zundel ion ($H_5O_2^+$), which provides a model for proton-assisted processes in aqueous solution. The corresponding reaction energy profile is shown in **Fig. 7**.

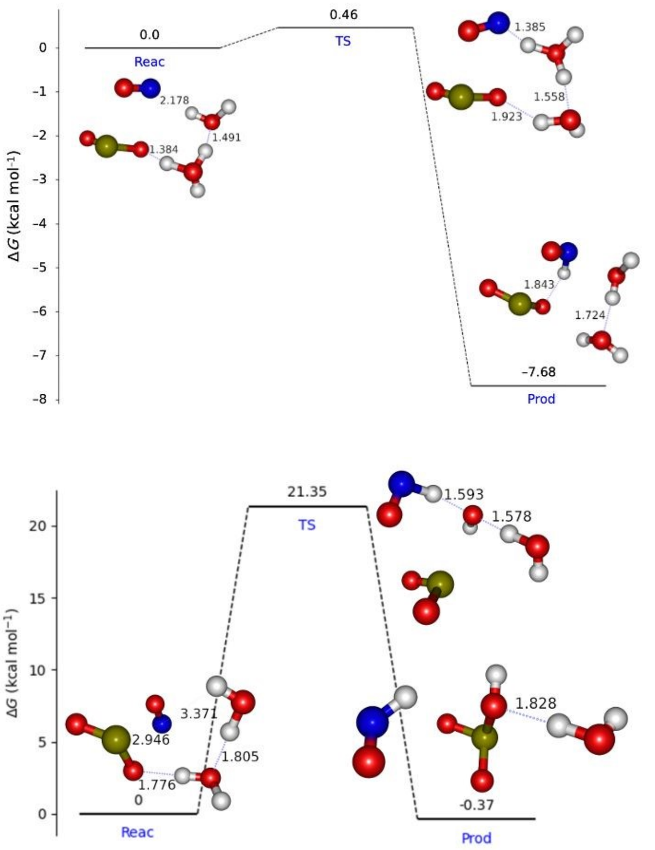

Fig. 7. Reaction Free Gibbs Energy (in kcal mol⁻¹) and optimized geometries for reactants (Reac), transition state (TS), and products (Prod) for the reaction $SO_2•^- + NO• + H_5O_2^+ \rightarrow HNO + 2H_2O + SO_2$ at the r²-SCAN(D4)/def2-TZVPP(SMD) level of theory: with the inclusion of the Zundel ion (upper panel); in the absence of explicit proton assistance (lower panel). In the absence of the H⁺, the products are HNO + H_2O + HSO_3^-

As shown in **Fig. 7**, inclusion of the Zundel ion markedly lowers the activation barrier, from 21.35 kcal mol⁻¹ in the absence of explicit proton assistance to 0.46 kcal mol⁻¹. In addition, the products of this reaction are stabilized by 7.68 kcal mol⁻¹ relative to the reactants in terms of standard Gibbs free energy. These results highlight the potential role of proton-assisted pathways in facilitating HNO formation within the broader reaction network depicted in **Fig. 5**.

Finally, to further rationalize the lag phase observed in N_2O formation (Fig. 2D), the interaction between NO• and $SO_2•^-$ was examined along the N–S coordinate. The one-dimensional electronic energy profile reveals a stabilization of approximately 15 kcal·mol⁻¹ as the two species approach each other from 3.0 to 2.1 Å (Fig. SI15). Such stabilization supports the formation of a relatively persistent intermediate species, which can act as a transient reservoir for nitrogen-containing intermediates. In this scenario, although dithionite consumption may proceed rapidly, the buildup of free HNO in solution is kinetically delayed, providing a mechanistic basis for the induction period observed experimentally.

Moreover, to further evaluate the role of protonation in triggering HNO release, we examined the protonated $SO_2NO^-·2H_2O$ adduct using a Zundel-type species. The corresponding transition state exhibits a single imaginary frequency (i286.48 cm⁻¹), whose associated displacement vectors do not lead toward HNO formation (Fig. SI16), but rather indicate structural reorganization within the $SO_2NO^-·2H_2O$ adduct. These results suggest that protonation of the intermediate does not directly promote HNO release, but instead contributes to its stabilization, reinforcing its role as a kinetic “delay agent” in the reaction pathway. Additionally, the possibility of partial reversibility in the early stages of the reaction cannot be excluded, which would further contribute to maintaining low effective concentrations of HNO during the initial phase.

Overall, the computational results support a mechanism in which the formation and stabilization of NO–SO_2-derived intermediates delays HNO release, and together with gas–liquid partitioning and equilibration of N_2O, accounts for the lag phase observed in the headspace N_2O signal.

Conclusions

In this work, we demonstrate that under anaerobic aqueous conditions at near-neutral pH, the reaction between sodium dithionite and NO• leads to the formation of HNO, which is subsequently converted into N_2O as the dominant nitrogen-containing end product. Both HNO and N_2O were experimentally detected, and product analysis indicates that more than 90% of the initial NO• is ultimately recovered as N_2O. These observations place dithionite-mediated NO• reduction within the broader redox landscape in which nitric oxide can access reduced nitrogen species, extending previous studies that focused mainly on comparatively mild reductants.

The extent and nature of NO• reduction were found to depend strongly on the relative concentrations of dithionite and NO•. Rather than converging to a single mechanistic pathway, the combined kinetic, spectroscopic, and computational results support a dynamic reaction network in which multiple nitrogen- and sulfur-centered species coexist and interconvert. Within this framework, HNO emerges as a chemically plausible and experimentally supported transient intermediate, without implying that it represents the sole reduced form of nitric oxide in the system. Direct reactions between sulfur-centered radical species and NO• may operate concurrently with proton-assisted and redox-coupled pathways, highlighting the intrinsic complexity of the chemistry involved.

Finally, given the high reactivity of HNO towards thiols and related functional groups, these findings have important implications for biochemical and enzymatic studies employing dithionite as a reductant. Unintended HNO formation may lead to modification or inhibition of thiol-containing enzymes, and such effects should be taken into consideration when interpreting experiments involving dithionite and nitric oxide under anaerobic or low-oxygen conditions.

View Article Online
DOI: 10.1039/D6DT00559D

Author contributions

P. V.: Methodology, Formal analysis, Data curation, Writing – original draft, review & editing. **M. F. V.** and **W. R. R.:** Methodology (computational), Formal analysis, Visualization, Writing – review. **S. A. S.** and **F. D.**: Conceptualization, Supervision, Funding acquisition, Writing – original draft, review & editing. All authors have read and agreed to the published version of the manuscript

Conflicts of interest

There are no conflicts to declare.

Data availability

The data supporting the findings of this study are available within the article and its Supplementary Information (SI). Additional data are available from the corresponding authors upon request. References[77–84] are cited in the SI.

Acknowledgements

This work was financially supported by the University of Buenos Aires (UBACYT 2023, 20020220100157BA Interacción entre NO y H_2S libres y coordinados a metales de transición, Director F.D.), the National Agency for the Promotion of Research, Technological Development, and Innovation (Interacciones entre tioles y H_2S con NO, libres y coordinados a metales de transición: posibles vías endógenas para la formación de HNO, PICT-2021-I-A-00745, Director F.D.), and CONICET (PhD fellowship to P.V.). W. R. R. would like to thank CNPq (Conselho Nacional de Desenvolvimento Científico e Tecnológico, Proc. 315507/2021-7) and FAPEMIG (Fundação de Amparo à Pesquisa do Estado de Minas Gerais, Proc. APQ-01942-24)) for the financial support and research grants. S.A.S. receives support from RYC2023-042682-I, funded by MCIU/AEI/10.13039/501100011033 and by the ESF+. F.D. is member of the research staff of CONICET.

References

1 R. G. Wilkins, *Kinetics and Mechanism of Reactions of Transition Metal Complexes*, Wiley, 1991.

2 K. Tsukahara and R. G. Wilkins, *J. Am. Chem. Soc.*, 1985, **107**, 2632–2635.

3 B. Milićević and G. Eigenmann, *Helv. Chim. Acta*, 1963, **46**, 192–197.

4 D. Lambeth and G. Palmer, *J. Biol. Chem.*, 1973, **248**, 6095–6103.

5 S. G. Mayhew, *Eur. J. Biochem.*, 1978, **85**, 535–547.

6 R. G. Rinker, T. P. Gordon, D. M. Mason, R. R. Sakaida and W. H. Corcoran, *J. Phys. Chem.*, 1959, **64**, 573–581.

7 C. Creutz and N. Sutin, *Inorg. Chem.*, 1974, **13**, 2041–2043.

8 L. Burlamacchi, G. Guarini and E. Tiezzi, *Trans. Faraday Soc.*, 1969, **65**, 496–503.

9 K. Jellinek, *Z. Phys. Chem.*, 1911, DOI:10.1515/zpch-1911-7624.

10 V. Münchow and R. Steudel, *Z. Anorg. Allg. Chem.*, 1994, **620**, 121–126.

11 W. J. Lem and M. Wayman, *Can. J. Chem.*, 1970, **48**, 776–781.

12 M. W. Lister and R. C. Garvie, *Can. J. Chem.*, 1959, **37**, 1567–1574.

13 V. L. Veguta, J. S. Stevanic, M. Lindström and L. Salmén, *BioResources*, 2017, **12**, 2496–2506.

14 K. Telfeyan, A. A. Migdisov, S. Pandey, V. V. Vesselinov and P. W. Reimus, *Appl. Geochem.*, 2019, **101**, 160–169.

15 I. A. Dereven'kov, D. S. Salnikov, S. V. Makarov, G. R. Boss and O. I. Koifman, *Dalton Trans.*, 2013, **42**, 15307–15314.

16 I. A. Dereven'kov and S. V. Makarov, *React. Kinet. Mech. Catal.*, 2020, **129**, 7–16.

17 K. K. Sen Gupta, N. Bhattacharjee and B. Pal, *Int. J. Chem. Kinet.*, 2016, **48**, 635–643.

18 M. Wolak, A. Zahl, T. Schneppensieper, G. Stochel and R. van Eldik, *J. Am. Chem. Soc.*, 2001, **123**, 9780–9791.

19 M. L. Quillin, T. Li, J. S. Olson, G. N. Phillips Jr., Y. Duo, M. Ikeda-Saito, R. Regan, M. Carlson, Q. H. Gibson, H. Li and R. Elber, *J. Mol. Biol.*, 1995, **245**, 416–436.

20 P. Ascenzi, G. De Simone, G. R. Tundo, C. Platas-Iglesias and M. Coletta, *J. Biol. Inorg. Chem.*, 2020, **25**, 361–370.

21 K. Nys, B. Cuypers, H. Berghmans, D. Hammerschmid, L. Moens, S. Dewilde and S. Van Doorslaer, *Biochim. Biophys. Acta Proteins Proteom.*, 2020, **1868**, 140413.

22 P. Ascenzi, G. De Simone, A. Pasquadibisceglie, M. Gioia and M. Coletta, *J. Inorg. Biochem.*, 2020, **214**, 111272.

23 E. G. Moore and Q. H. Gibson, *J. Biol. Chem.*, 1976, **251**, 2788–2794.

24 S. Van Doorslaer, S. Dewilde, L. Kiger, S. V. Nistor, E. Goovaerts, M. C. Marden and L. Moens, *J. Biol. Chem.*, 2003, **278**, 4919–4925.

25 M. Brunori, A. Giuffrè, K. Nienhaus, G. U. Nienhaus, F. M. Scandurra and B. Vallone, *Proc. Natl. Acad. Sci. U. S. A.*, 2005, **102**, 8483–8488.

26 S. Carballal, E. Cuevasanta, P. K. Yadav, C. Gherasim, D. P. Ballou, B. Alvarez and R. Banerjee, *J. Biol. Chem.*, 2016, **291**, 8004–8013.

27 R. Grubina, S. Basu, M. Tiso, D. B. Kim-Shapiro and M. T. Gladwin, *J. Biol. Chem.*, 2008, **283**, 3628–3638.

28 S. A. Suarez, P. Vargas and F. A. Doctorovich, *J. Inorg. Biochem.*, 2021, **216**, 111333.

29 C. M. Gallego, A. Mazzeo, P. Vargas, S. Suárez, J. Pellegrino and F. Doctorovich, *Chem. Sci.*, 2021, **12**, 10410–10425.

30 S. A. Suarez, *Redox Biochem. Chem.*, 2024, **8**, 100024.

31 P. Vargas, F. A. Doctorovich and S. A. Suarez, *Eur. J. Inorg. Chem.*, 2024, **27**, e202400190.

32 M. Arasimowicz-Jelonek, J. Floryszak-Wieczorek, S. Suarez, F. Doctorovich, E. Sobieszczuk-Nowicka, S. Bruce King, G. Milczarek, T. Rębiś, J. Gajewska, P. Jagodzik and M. Żywicki, *Nat. Plants*, 2022, **9**, 36–44.

33 R. W. Voland, H. Wang, H. D. Abruña and K. M. Lancaster, *Proc. Natl. Acad. Sci.*, 2025, **122** (3) e2416971122.

34 C. Van Stappen, L. E. Goodrich and N. Lehnert, in *The Chemistry and Biology of Nitroxyl (HNO)*, eds. F. Doctorovich, P. J. Farmer and M. A. Martí, Elsevier, Amsterdam, 2017, pp. 155–192.

35 K. Fujisawa, T. Kataoka, K. Terashima, H. Kurihara, F. de Santis Gonçalves and N. Lehnert, *Molecules*, 2023, **28**, 6206.

36 N. Lehnert, E. Kim, H. T. Dong, J. B. Harland, A. P. Hunt, E. C. Manickas, K. M. Oakley, J. Pham, G. C. Reed and V. S. Alfaro, *Chem. Rev.*, 2021, **121**, 14682–14905.

37 C. Ferousi, S. H. Majer, I. M. DiMucci and K. M. Lancaster, *Chem. Rev.*, 2020, **120**, 5252–5307.

38 J. M. Fukuto, *Br. J. Pharmacol.*, 2019, **176**, 135–146.

39 N. Paolocci, G. Keceli, D. A. Wink and D. A. Kass, in *The Chemistry and Biology of Nitroxyl (HNO)*, eds. F. Doctorovich, P. J. Farmer and M. A. Martí, Elsevier, Amsterdam, 2017, pp. 353–387.

40 R. Michalski, R. Smulik-Izydorczyk, J. Pięta, M. Rola, A. Artelska, K. Pierzchała, J. Zielonka, B. Kalyanaraman and A. B. Sikora, *Front. Chem.*, 2022, **10**, 930657.

41 S. A. Plano, F. M. Baidanoff, L. L. Trebucq, S. A. Suarez, F. Doctorovich, D. A. Golombek and J. J. Chiesa, *Molecules*, 2021, **26**, 2514.

42 K. M. Miranda, A. S. Dutton, L. A. Ridnour, C. A. Foreman, E. Ford, N. Paolocci, T. Katori, C. G. Tocchetti, D. Mancardi, D. D. Thomas, M. G. Espey, K. N. Houk, J. M. Fukuto and D. A. Wink, *J. Am. Chem. Soc.*, 2005, **127**, 722–731.

43 F. T. Bonner and B. Ravid, *Inorg. Chem.*, 1975, **14**, 558–563.

44 R. Smulik-Izydorczyk, J. Pięta, R. Michalski, M. Rola, K. Kramkowski, A. Artelska, J. Zielonka and A. B. Sikora, *Redox Biochem. Chem.*, 2024, **8**, 100031.

45 N. I. Neuman, M. F. Venâncio, W. R. Rocha, D. E. Bikiel, S. A. Suárez and F. Doctorovich, *Inorg. Chem.*, 2021, **60**, 15997–16007.

46 S. Suarez, J. Floryszak-Wieczorek, E. Sobieszczuk-Nowicka, F. Doctorovich and M. Arasimowicz-Jelonek, *J. Exp. Bot.*, 2025, **76**, 3809–3822.

47 R. Smulik-Izydorczyk, K. Dębowska, M. Rostkowski, J. Adamus, R. Michalski and A. Sikora, *Cell Biochem. Biophys.*, 2021, **79**, 845–856.

48 M. E. Shoman, J. F. Dumond, T. S. Isbell, J. H. Crawford, A. Brandon, J. Honovar, D. A. Vitturi, C. R. White, R. P. Patel and S. B. King, *J. Med. Chem.*, 2011, **54**, 1059–1070.

49 T. W. Miller, M. M. Cherney, A. J. Lee, N. E. Francoleon, P. J. Farmer, S. B. King, A. J. Hobbs, K. M. Miranda, J. N. Burstyn and J. M. Fukuto, *J. Biol. Chem.*, 2009, **284**, 21788–21796.

50 M. Hamer, S. A. Suarez, M. Muñoz, L. Álvarez, M. Martí and F. Doctorovich, *Pure Appl. Chem.*, 2020, **92**, 2005–2014.

51 R. Sander, *Atmos. Chem. Phys.*, 2015, **15**, 4399–4981.

52 I. G. Zacharia and W. M. Deen, *Ann. Biomed. Eng.*, 2005, **33**, 214–222.

53 J. L. Heinecke, C. Khin, J. C. M. Pereira, S. A. Suárez, A. V. Iretskii, F. Doctorovich and P. C. Ford, *J. Am. Chem. Soc.*, 2013, **135**, 4007–4017.

54 C. Fehling and G. Friedrichs, *J. Am. Chem. Soc.*, 2011, **133**, 17912–17922.

55 G. Carrone, A. Mazzeo, E. Marceca, J. Pellegrino, S. Suárez, J. Zarenkiewicz, J. P. Toscano and F. Doctorovich, *J. Inorg. Biochem.*, 2021, **223**, 111535.

56 L. Álvarez, S. A. Suárez, P. J. González, C. D. Brondino, F. Doctorovich and M. A. Martí, *Inorg. Chem.*, 2020, **59**, 7939–7952.

57 M. A. Martí, S. E. Bari, D. A. Estrin and F. Doctorovich, *J. Am. Chem. Soc.*, 2005, **127**, 4680–4684.

58 I. Boron, S. A. Suárez, F. Doctorovich, M. A. Martí and S. E. Bari, *J. Inorg. Biochem.*, 2011, **105**, 1044–1049.

59 F. Doctorovich, D. E. Bikiel, J. Pellegrino, S. A. Suarez and M. A. Marti, in *Prog. Inorg. Chem.*, Elsevier, 2014, **58**, 145–183.

60 M. E. R. Pschepiurca, N. Vadra and S. A. Suarez, *Eur. J. Inorg. Chem.*, 2023, **26**, e202300005.

61 F. Doctorovich, D. E. Bikiel, J. Pellegrino, S. A. Suárez and M. A. Martí, in *Adv. Inorg. Chem.*, 2012, **64**, 97–139.

62 F. Weigend, *Phys. Chem. Chem. Phys.*, 2006, **8**, 1057–1065.

63 E. Caldeweyher, S. Ehlert, A. Hansen, H. Neugebauer, S. Spicher, C. Bannwarth and S. Grimme, *J. Chem. Phys.*, 2019, **150**, 154122.

64 A. V. Marenich, C. J. Cramer and D. G. Truhlar, *J. Phys. Chem. B*, 2009, **113**, 6378–6396.

65 F. Neese, *Wiley Interdiscip. Rev. Comput. Mol. Sci.*, 2012, **2**, 73–78.

66 J. W. C. Johns, A. R. W. McKellar and E. Weinberger, *Can. J. Phys.*, 1983, **61**, 1106–1119.

67 H. W. Brown and G. C. Pimentel, *J. Chem. Phys.*, 1958, **29**, 883–888.

68 M. Yan, J. C. Lo, J. T. Edwards and P. S. Baran, *J. Am. Chem. Soc.*, 2016, **138**, 12692–12714.

69 P. T. Lynch, C. J. Annesley, C. J. Aul, X. Yang and R. S. Tranter, *J. Phys. Chem. A*, 2013, **117**, 4750–4761.

70 S. Bebe, X. Yu, R. A. Hutchinson and L. J. Broadbelt, *Macromol. Symp.*, 2006, **243**, 179–189.

71 NDRL/NIST Solution Kinetics Database, https://kinetics.nist.gov/solution/.

72 M. Bringas, J. Semelak, A. Zeida and D. A. Estrin, *J. Inorg. Biochem.*, 2016, **162**, 102–108.

73 F. Camacho, M. P. Pfiez, M. C. Jiménez and M. Fernández, *Application of the Sodium Dithionite Oxidation to Measure Oxygen Transfer Parameters*, 1997, **52**.

74 J. A. Morello, M. R. Craw, H. P. Constantine and R. E. Forster, *J. Appl. Physiol.*, 1964, **19**, 522–525.

75 R. E. Huie, C. L. Clifton and N. Altstein, *Radiat. Phys. Chem.*, 1989, **33**, 361–370.

76 W. Xing, M. Yin, Q. Lv, Y. Hu, C. Liu and J. Zhang, in *Rotating Electrode Methods and Oxygen Reduction Electrocatalysts*, Elsevier, 2014, pp. 1–31.

77 N. N. Greenwood and A. Earnshaw, *Chemistry of the Elements*, 2nd edn., 1997.

78 J. E. House and K. A. House, *Descriptive Inorganic Chemistry*, 3rd edn., Elsevier, 2016.

79 S. V. Lymar, V. Shafirovich and G. A. Poskrebyshev, *Inorg. Chem.*, 2005, **44**, 5212–5221.

80 P. L. Fernandez and A. S. Murkin, *Molecules*, 2020, **25**, 1933.

81 C. E. Housecroft and A. G. Sharpe, *Inorganic Chemistry*, 4th edn., 2012.

82 J. Katz, *Am. Sci.*, 1960, **48**, 544–580.

83 L. J. Altman, P. Laungani, G. Gunnarsson, H. Wennerström and S. Forsén, *J. Am. Chem. Soc.*, 1978, **100**, 8264–8266.

84 S. Scheiner and M. Čuma, *J. Am. Chem. Soc.*, 1996, **118**, 1511–1521.

View Article Online
DOI: 10.1039/D6DT00559D

View Article Online
DOI: 10.1039/D6DT00559D

The data supporting the findings of this study are available within the article and its Supplementary Information (SI). Additional data are available from the corresponding authors upon request. References77–84 are cited in the SI.